Higher order mode beams mitigate halos in high intensity proton linacs

Abhishek Pathak and Srinivas Krishnagopal

Ion Accelerator Development Division, Bhabha Atomic Research Centre, Mumbai 400 085, India

(Received 8 February 2016; published 3 January 2017)

High intensity proton linacs (HIPLs) for applications such as Accelerator Driven Reactor Systems (ADRS) have serious beam dynamics issues related to beam halo formation. This can lead to particle loss and radioactivation of the surroundings which consequently limit the beam current. Beam halos are largely driven by the nonlinear space-charge force of the beam, which depends strongly on the beam distribution and also on the initial beam mismatch. We propose here the use of a higher order mode beam (HOMB), that has a weaker nonlinear force, to mitigate beam halos. We first show how the nonlinear space-charge force can itself be exploited in the presence of nonlinear solenoid fields, to produce a HOMB in the low energy beam transport (LEBT) line. We then study the transport of such a beam through a radio frequency quadrupole (RFQ), and show that the HOMB has a significant advantage in terms of emittance blow-up, halo formation and beam loss, over a Gaussian beam, even with a finite initial mismatch. For example, for the transport of a 30 mA beam through the RFQ, with an initial beam mismatch of 45%, the Gaussian beam sees an emittance blow-up of 125%, while the HOMB sees a blow-up of only 35% (relative to the initial emittance of 0.2π mm-mrad). Similarly, the beam halo parameter and beam loss are 0.95 and 25% respectively for a Gaussian beam, but only 0.35 and 15% for a HOMB. The beam dynamics of the HOMB agrees quite well with the particle-core model, because of the more linear space-charge force, while for the Gaussian beam there are additional particle loss mechanisms arising from nonlinear resonances. Therefore, the HOMB suppresses emittance blow-up and halo formation, and can make high current ADRS systems more viable.

DOI: 10.1103/PhysRevAccelBeams.20.014201

I. INTRODUCTION

High intensity proton linacs (HIPLs) are necessary for many applications such as spallation neutron sources [1,2] and neutrino production [3], and in Accelerator Driven Reactor Systems (ADRS) for energy production [4], waste transmutation [5], and thorium production [6]. The typical average beam currents required for these applications are many mAs, and for ADRS even 10s of mAs. With such intense beams, the nonlinear Coulomb repulsion or space-charge force is very strong, and can lead to the production of *beam halos*, i.e. diffusion of particles to large distances from the center. This is an important concern in HIPLs, because these halo particles will be lost at the walls of the vacuum chamber, resulting in radioactivation of the chamber and surroundings, which is a significant safety concern that can limit the maximum operating beam current.

Beam halos have been studied with a variety of theoretical [7–12], computational [13,14] and experimental [15–18] tools. Theoretical studies have used a core-particle model [19,20] to study the dynamics of halo particles in the presence of initial beam mismatch, but assume a uniform beam core, which implies a linear space-charge force. Particle-In-Cell (PIC) simulations [21–24] have found that beam halos are formed at low energies, when the nonlinear space-charge force is stronger, in the presence of initial beam mismatch. Some experiments on beam halos have been carried out at the Low Energy Demonstration Accelerator (LEDA) [10]. Their observations differed from theoretical predictions using the particle-core model, and led to a modified theoretical model to explain beam halos [10]. The practical outcome of these various studies is that from the requirement of controlling radioactivation to a level that allows periodic maintenance to be carried out, it is necessary to restrict beam loss to around 1 nA/m at an energy of 1 GeV. For a 30 mA proton beam, this corresponds to controlling beam loss to a level of 30 parts per billion. Clearly, this is a very challenging task, and requires detailed beam dynamics studies to develop an understanding of halo formation, and to devise ways and means of controlling or mitigating these halos.

The high current proton beam generated from an ion source is usually transported, through a low energy beam transport (LEBT) system, to a radio-frequency quadrupole (RFQ) that is the first accelerating structure in modern proton linacs. In the LEBT the proton beam is at its lowest energy, typically 10s of keV, and the space-charge force is at its greatest, but since there is no accelerating structure it

is possible to employ the technique of *space-charge compensation* [25], to reduce the space-charge force by as much as 95%. However, once the beam enters the RFQ it is not possible to employ this technique, and one may expect substantial emittance blow-up as well as halo formation, which will lead to beam loss. Since the fundamental driver of halo formation is the space-charge force, in looking for ways of mitigating halo formation, it is interesting and relevant to look at ways of reducing the space-charge force, especially at lower energies. One way to modify the space-charge force, for a given charge or current, is to modify the charge distribution of the beam.

In this paper we propose a novel idea of generating and employing a higher order Laguerre-Gauss (LG) beam distribution [26], in which the peak of the charge density is not at the center but at a finite radius. Such a *higher-order mode beam* (HOMB) would have a more linear space-charge force compared to a Gaussian, and would therefore be more favorable for halo mitigation. In fact, current limits in hollow beams have been studied before [27,28], though not with a view to generating them in an LEBT or using them for transport through an RFQ to mitigate beam halos. We first show, using three-dimensional particle-in-cell (PIC) simulations, how the nonlinear space-charge force of the beam, in the presence of the nonlinear solenoid fields of the LEBT, can itself be exploited to produce a HOMB. We emphasize that this beam does not have zero particle density at the center and is therefore not a pure LG_{01} mode; in fact, we show that it is a combination of $LG_{00} + LG_{01} + LG_{02}$. We then show that in the subsequent transport of a high (30 mA) current proton beam through the RFQ the HOMB has substantially less emittance blow-up, tune depression, and halo formation and is more tolerant to initial mismatch, compared to a Gaussian beam. Detailed tracking studies show that a large fraction of the lost particles originate from the center of the beam, and since the HOMB has fewer particles at the center, it explains why there is less beam loss. Our results for the HOMB, which has a more linear space-charge force, agree well with the prediction of the particle-core model that halos are driven by the 1:2 (particle to envelope) parametric resonance. For the Gaussian beam, however, we show that transverse nonlinear resonances provide an additional mechanism for halo and emittance growth and particle loss, and consequently lead to poorer beam dynamics.

II. PRODUCTION OF A HIGHER ORDER MODE BEAM (HOMB)

We first show how a HOMB can be generated in the LEBT of a HIPL. Figure 1 shows a schematic of the beamline transporting beam from a 50 keV, 30 mA proton ion source, through a LEBT to the RFQ; the parameters were chosen in conformity with the requirements of the ADRS system being studied and designed at our center

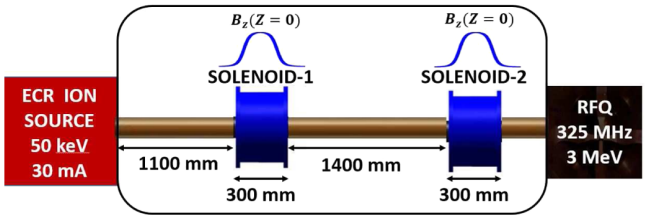

FIG. 1. Schematic of the beamline transporting a 50 keV, 30 mA proton beam from the ion source to the 3 MeV RFQ.

[29]. The LEBT comprises two magnetic solenoids with drift spaces before, in-between and after the solenoids. The magnetic strengths were varied to match the beam ellipse to the acceptance of the RFQ. An axisymmetric, 50 keV, 30 mA, DC Gaussian (4σ) beam was initialized at the entrance of the LEBT, with a rms normalized emittance of 0.2π mm-mrad and with Twiss parameters [30,31] $\alpha = -1.8$ and $\beta = 0.24$ mm. The field profile for the solenoids was taken from measurements made on an actual LEBT solenoid, though assumed identical for both solenoids, in order to have a more realistic field. The simulations were performed with the code TRACEWIN [32]. In all our simulations the number of macroparticles ($\geq 10^7$) as well as the number of time steps ($\geq 100/\beta\lambda$) were kept large enough to ensure numerical convergence. Space-charge compensation of 95% was implemented using the ionization potential given in Ref. [25] that leads to an effective current of 1.5 mA. The solenoid strengths were then varied to match the Twiss parameters (α, β, γ) with the acceptance of the RFQ.

As one would expect for a Gaussian beam with its strong nonlinearity, the beam radius blows up from 10 mm to 100 mm before getting focused by the solenoids and we finally obtained a beam with a spot size of 5 mm and an rms normalized emittance of 0.36π mm-mrad at the exit of the LEBT. For an initial Gaussian beam we find that at lower values of the current the transverse particle distribution at the exit of the LEBT remains close to Gaussian, but as we raise the current the particle density at the center first flattens out, and as we cross a threshold value of 700 μA the beam starts becoming hollow, as shown in Fig. 2(a), with the density at the center being around half the density at the peak. We also observe that the process of hollowing

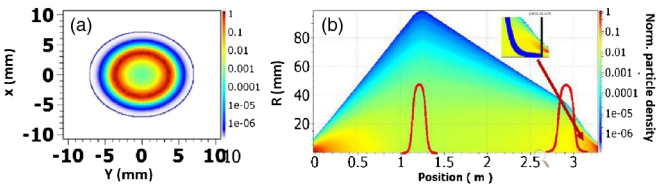

FIG. 2. (a) Transverse particle density distribution of the proton beam at the exit of the LEBT, (b) *r-z* particle density plot in the LEBT, showing the formation of the hollow beam in the nonlinear solenoid field.

out of the beam begins in the nonlinear fringe field region of the solenoid, as shown in Fig. 2(b). Thus, the nonlinear space-charge force itself, in the presence of a nonlinear solenoid field, provides a way of generating a HOMB.

Figure 3 shows the particle density as a function of the transverse coordinate x (for $y = 0$), where the non-Gaussian nature of the distribution can be seen more clearly. Also shown are fits to this distribution using the first few higher-order Laguerre-Gauss modes: LG_{01}, $LG_{00} + LG_{01}$, and $LG_{00} + LG_{01} + LG_{02}$. The electric field E_{lm} of the Laguerre-Gauss modes is given by,

$$E_{lm}(r,\phi,z) = \frac{C_{lm}}{w(z)} e^{\left[\frac{-r^2}{w^2(z)}\right]} \times e^{-i\alpha}(-1)^{\min(l,m)} \times \left[\frac{r\sqrt{2}}{w(z)}\right]^{l-m} L^{l-m}_{\min(l,m)}\left[\frac{2r^2}{w^2(z)}\right], \quad (1)$$

where L^l_p is the Laguerre polynomial, $w(z)$ is the transverse beam size and C_{lm} is a constant. Here,

$$\alpha = K\frac{r^2}{2w(z)} + (l+m+1)\psi + (l-m)\phi, \quad (2)$$

and,

$$\psi = \tan^{-1}\left(\frac{z}{z_R}\right), \quad (3)$$

where z_R is the Rayleigh range and K is a constant.

It can be seen that a combination of the three lowest modes fits the distribution extremely well. Therefore, the observed beam distribution at the exit of the LEBT can justifiably be described as a HOMB.

Formation of such a HOMB or hollow beam has been reported before for multi-species heavy-ion accelerators such as FRIB at Michigan [33], RIA at Michigan [34], and Linac3 at CERN [35] but not for high intensity proton accelerators. In Ref. [35] the formation of hollow uranium beams is explained as a consequence of the space-charge effect of tightly focused beams with higher charge to mass ratio, and leads to strong emittance blow up in the uranium beam. In our case, there is no additional beam to provide this external force, and the proton beam is not at a focal point when it turns hollow. Most importantly, as we show below, transition to a hollow beam, or HOMB, is not accompanied by emittance blow up.

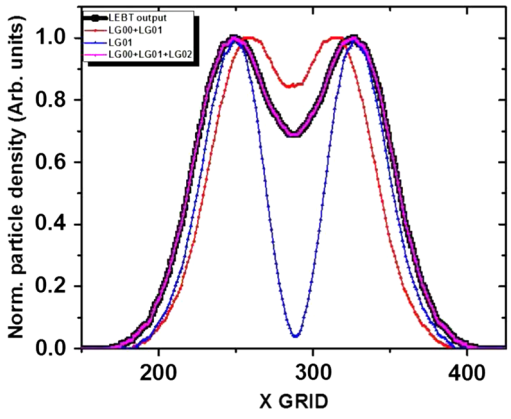

FIG. 3. Line-out of the horizontal density distribution of the HOMB, along with fits to various higher-order Laguarre-Gauss modes.

Clearly, the formation of a HOMB is driven by the nonlinear force experienced by the particles; they take up a distribution that minimizes the force. However there are two potential sources of this nonlinearity. One is the nonlinear space-charge force and the other is the nonlinear field of the solenoid magnets. It is not obvious that one or the other of these two forces predominates. Therefore, in order to understand these issues better, we performed a systematic study with different initial beam distributions, corresponding to different degrees of nonlinearity in the space-charge force. We considered four different beam distributions: Gaussian, parabolic, 4D water-bag, and KV [36]. Explicitly, the fields for the different distributions are,

$$E(r) = \frac{Ir}{2\pi\epsilon_0 R^2\beta c} \quad (4)$$

for KV,

$$E(r) = \frac{2Ir}{3\pi\epsilon_0 R^2\beta c}\left(1 - \frac{r^2}{3R^2}\right) \quad (5)$$

for 4D water-bag,

$$E(r) = \frac{3Ir}{4\pi\epsilon_0 R^2\beta c}\left(1 - \frac{r^2}{2R^2} + \frac{r^4}{12R^4}\right) \quad (6)$$

for parabolic, and,

$$E(r) = \frac{I}{2\pi\epsilon_0 r\beta c}(1 - e^{-2\frac{r^2}{R^2}}) \quad (7)$$

for Gaussian. Here I is the beam current, R is the beam size, r is the radial distance from the center, and β is the relativistic factor.

In each case, we varied the space-charge compensated beam current from 100 μA to 1.5 mA in steps of 100 μA (corresponding to an uncompensated current varied from 2 mA to 30 mA in steps of 2 mA), to vary the strength of the space-charge nonlinearity. For an initial Gaussian beam, we find that at lower values of the current, the transverse particle distribution at the exit of the LEBT remains close to Gaussian, but as we raise the current the particle density at the center first flattens out, and as we cross the threshold

value of 700 μA the beam starts becoming hollow, i.e. a HOMB. We repeated the same study for parabolic, water-bag and KV distributions, where each of them carries a different degree of nonlinearity in the space-charge force. We found that for all three distributions we do get a HOMB, at current thresholds of 800 μA, 1 mA, and 1.1 mA, respectively. It is therefore clear that both the beam intensity and nature of space charge field contribute to making the beam hollow, but at different current thresholds depending on the initial distribution. The greater the degree of nonlinearity, the lower the threshold for the production of a hollow beam.

An important issue that needs to be addressed is if the emittance of the beam changes abruptly when the beam distribution transitions to a HOMB. Figure 4(a) shows a plot of the beam emittance at the end of the LEBT as a function of the beam current, for all four beam distributions. In each case, the range of currents straddles the threshold current above which the beam becomes a HOMB.

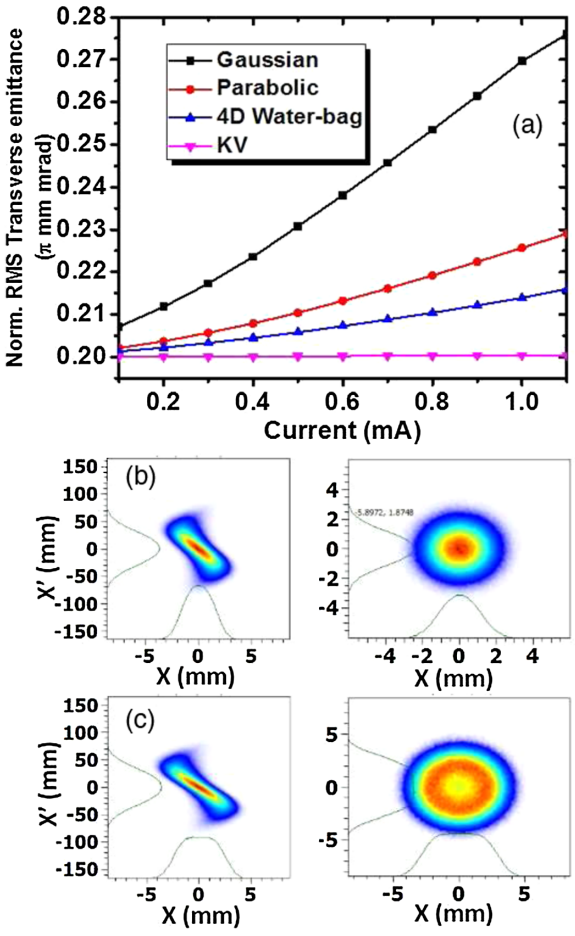

FIG. 4. (a) Normalized emittance (RMS) at the LEBT output as a function of the (compensated) beam current, for four different beam distributions, (b) phase space (left) and coordinate space (right) distributions at the LEBT exit for an initial Gaussian beam of current 500 μA (below threshold) and (c) phase space (left) and coordinate space (right) distributions at the LEBT exit for an initial Gaussian beam of current 800 μA (above threshold).

It can be seen that the variation of emittance with current is smooth for all four beam distributions, with no abrupt change at the threshold current, in spite of the change in the beam distribution. Figures 4(b) and 4(c) show the phase-space and coordinate space distributions at the end of the LEBT, for an initial Gaussian distribution, for a current of 500 μA (below threshold) and 800 μA (above threshold), respectively. It can be seen clearly that while the coordinate space plots are completely different above and below threshold, and show that the beam is Gaussian below threshold but HOMB above threshold, there is not much difference in the phase space plots.

To better understand the HOMB formation, we looked at the radius of the peak of the density distribution of the HOMB (see Fig. 3) as a function of beam current, for all four initial beam distributions, Fig. 5. For all four distributions this radius keeps increasing as the beam current increases, though with different slopes. The slope is steepest for the Gaussian distribution followed by parabolic, waterbag, and KV, respectively. At our operating current of 1.5 mA, the value of this radius is 4.2 mm, 3.4 mm, 1.5 mm, and 1.1 mm, for Gaussian, parabolic, waterbag, and KV distributions, respectively. Once can try to calculate the value of this radius of maximum density through a simple argument. Though the mechanism of formation of the HOMB may depend on the details of complex nonlinear forces, in essence the particles in the beam see a radially outward space-charge force and an effective radially inward solenoid force. Where these two forces are equal, there will be no net force on the particle and so it will be in equilibrium and therefore one may expect the maximum particle density at this value of the radius. To check this, both the space-charge and solenoid forces were calculated and compared at the point of formation of the hollow beam for different beam currents, Fig. 6. For a given current, the value of the radial distance at

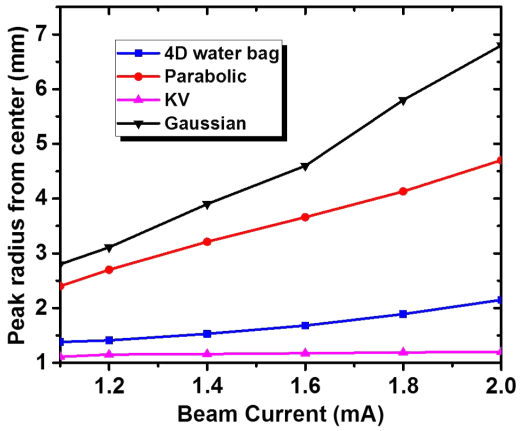

FIG. 5. Variation of the radius of the peak of the density distribution of the HOMB, for Gaussian, parabolic and 4D waterbag and KV initial distributions, as a function of beam current.

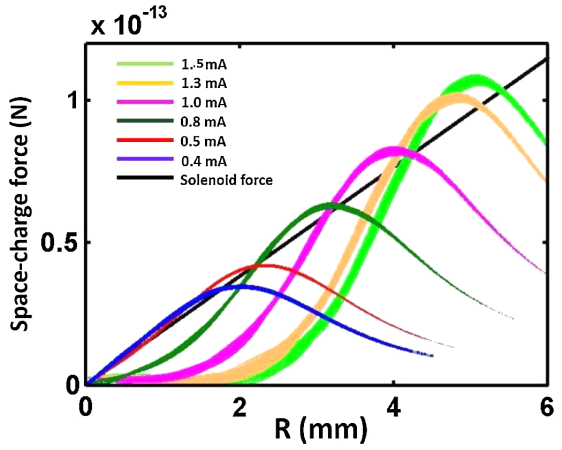

FIG. 6. Variation of the space-charge force along the radial direction for a Gaussian beam for different beam current superposed with the solenoid force along the radial direction, at the point of formation of the HOMB.

which the two curves (one for the space charge force at that current and the other the straight line for the solenoid) intersect, gives the value of the radius of maximum density—we take the first intersection since the second intersection is at a larger radius, where there are fewer particles. For a current of 1.5 mA and an initial Gaussian beam, this value is around 4.2 mm—which agrees very well with the value of 4.2 mm, quoted above, obtained from the actual beam distribution.

III. BEAM TRANSPORT THROUGH THE RFQ

Beam transport through the RFQ is a bigger issue than through the LEBT, because in the RFQ space-charge compensation cannot be implemented, and therefore one has to deal with the full space-charge force; in our case due to a very intense, 30 mA, beam. The particle-core model suggests that the major factor determining halo growth is diffusion of particles from the core as a result of a particle-core transverse parametric resonance. With the introduction of mismatch in the initial Twiss parameters, the core becomes unstable, leading to envelope oscillations. Since we are initializing an axisymmetric DC beam at the entrance to the RFQ we expect only the breathing mode [20] with a frequency $\sigma_{\mathrm{env}.H} = \sqrt{\sigma_{0,t}^2 + \sigma_t^2}$, where $\sigma_{0,t}$ is the zero current phase advance and σ_t is the full current phase advance. This is followed by Landau damping of the core oscillations, resulting in transfer of energy to the particles, thus driving halo formation.

To study the beam dynamics through the RFQ, we used the fully three-dimensional PIC code TOUTATIS (with 64 steps per $\beta\lambda$ and 10^5 macroparticles). We studied two different initial beam distributions: one the HOMB obtained at the exit of the LEBT, as discussed above, and the other a freshly generated Gaussian beam with Twiss parameters and emittance identical to that of the HOMB at the same location. (Using the same emittance for the Gaussian beam is justified from Fig. 4, as discussed above.) Simulations were performed for the RFQ designed for the Low Energy High Intensity Proton Accelerator (LEHIPA) that takes a 50 keV beam from the LEBT and accelerates it to 3 MeV over a distance of 4 m, with an average vane radius of 3.63 cm and an inter-vane voltage of 68 kV [37]. Simulations were performed for beams with the Twiss parameters matched to the RFQ, as well as with an equal mismatch in the Twiss parameters (up to 45%) with the relation,

$$\alpha_{mx}(0) = \alpha_{my} = (1+M)^2 \times \alpha_x(0) \tag{8}$$

and

$$\beta_{mx}(0) = \beta_{my} = (1+M)^2 \times \beta_x(0), \tag{9}$$

where M is the mismatch introduced and α, β are the Twiss parameters.

Figure 7(a) shows the variation of the rms normalized transverse emittance of the Gaussian and HOMB beams at the exit of the RFQ with different mismatch percentages, both starting with an emittance of 0.36π mm-mrad at the RFQ input. For the Gaussian beam the emittance increases further to 0.39π mm-mrad, for zero mismatch and keeps increasing as the value of mismatch increases, reaching an emittance of 0.45π mm-mrad for 45% mismatch. On the other hand for the HOMB the emittance actually decreases to 0.26π mm-mrad without any mismatch; even with a mismatch of 45% the emittance decreases, to 0.27π mm-mrad. Figure 7(b) shows that the transverse beam halo parameter [9] increases monotonically with increase in the mismatch and is always much higher for the Gaussian (0.85–0.95) than for the HOMB (0.32 to 0.35). Similarly the percentage beam loss without mismatch are 10% and 4% for the Gaussian and HOMB, respectively, and with a mismatch of 45% these increase to 25% and 15%, respectively.

We also looked at the possible effect of the longitudinal dynamics on beam quality and beam loss. Figure 7(c) shows the normalized rms longitudinal emittance with different degrees of initial beam mismatch for the Gaussian and HOMB. For no mismatch the longitudinal emittances for the Gaussian and HOMB are 0.408 and 0.387π mm-mrad respectively, and increase to 0.419 and 0.395π mm-mrad, respectively, for an initial mismatch of 45%. Thus, there is no significant difference in the longitudinal emittance of the Gaussian and HOMB, unlike the case of the transverse emittance. This shows that there is no emittance exchange between the longitudinal and transverse dimensions. Similarly, we also looked at the longitudinal halo for both distributions at the RFQ exit [Fig. 7(d)]. For an ideal matched beam the halo parameters

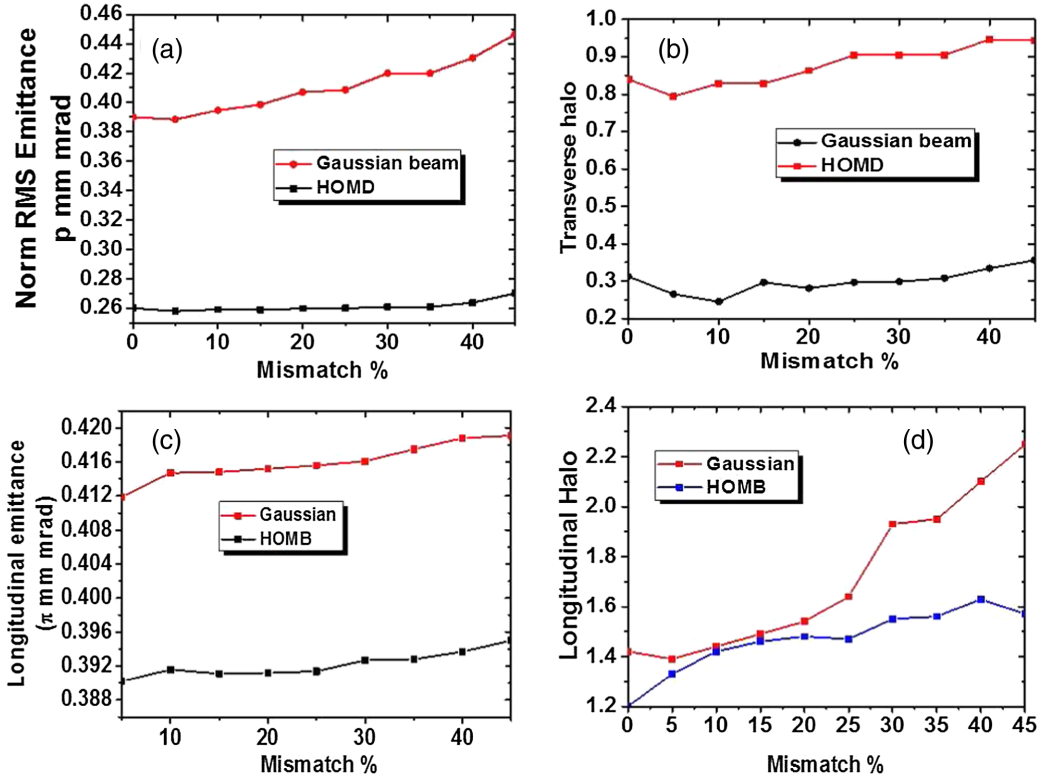

FIG. 7. For the Gaussian and HOMB distributions, variation as a function of initial beam mismatch of, (a) transverse emittance, (b) transverse halo parameter, (c) longitudinal emittance, and (d) longitudinal halo parameter, all calculated at the exit of the RFQ.

for the Gaussian and HOMB are 1.42 and 1.2, respectively, and with the introduction of mismatch in the transverse plane they increase, reaching values of 2.25 and 1.57, respectively, for a mismatch of 45%.

Tracking individual particle trajectories shows that the percentage of particles escaping the longitudinal separatrix is not more than 1.5% and 1% for the Gaussian and HOMB, respectively. However, the percentage increases with mismatch in the input beam to values of 1.5% and 1.1%, respectively, for an initial mismatch of 45%.

Another parameter that characterizes the space-charge nonlinearity is the *tune depression*, defined as the ratio of full current to zero current phase advances (focusing forces). Figure 8 shows the tune depression for both distributions along the length of the RFQ. One can clearly see a significant depression (less than 0.6) of the tune for the Gaussian beam, while for the HOMB it is well above 0.75. Thus, in terms of transverse beam emittance, beam halo and tune depression, the HOMB produces much better beam quality than the Gaussian.

Some features of the emittance blow-up in the RFQ are in consonance with the predictions of the particle-core model. This can be seen from Figs. 9(a) and 9(b) that show the envelope oscillations and the rms normalized emittance down the length of the RFQ, for the Gaussian and HOMB and for a mismatch of 30%. Without mismatch, the envelope will just show betatron oscillations at a single frequency. Mismatch introduces envelope modulations at a lower frequency. Figure 9(a) shows the ratio of the envelope size with mismatch to the size without mismatch. It can be seen that for both initial distributions the envelope oscillations break out immediately. For the Gaussian beam these oscillations are Landau damped quickly, within the first 50 cm of the RFQ. As a result, over this distance energy is transferred to the particles which blow out, and the emittance blows up, as can be seen from Fig. 9(b). Beyond that the slight decrease in emittance is because

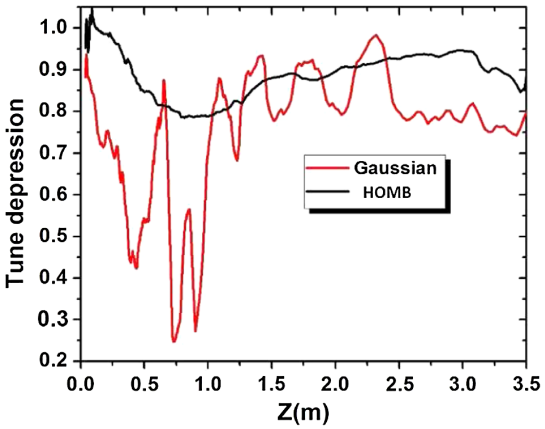

FIG. 8. Tune depression for the Gaussian and HOMB along the RFQ.

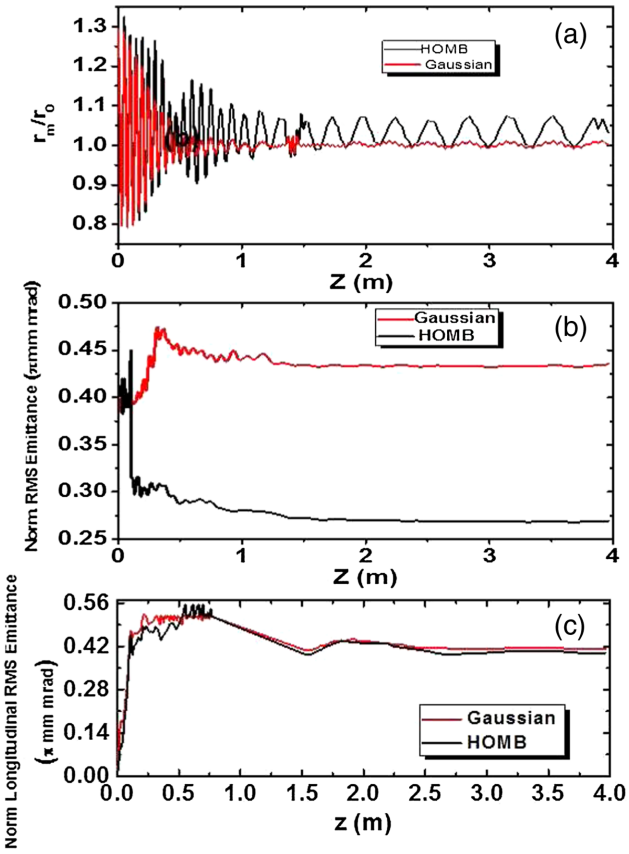

FIG. 9. (a) Damping of the envelope oscillations, and (b) growth of the transverse rms normalized emittance, along the RFQ, for an initial mismatch of 30% and (c) growth of rms longitudinal emittance along RFQ for the mismatch of 30%.

some of the halo particles are lost. For the HOMB, the oscillations do start damping out initially, as a consequence of which the emittance blows up, but subsequently the oscillations start back up before settling to a uniform frequency. This is indicative of the fact that the particles must actually be giving up energy to the core, as a result of which the emittance now reduces. In addition, there is particle loss in this region (discussed in greater detail later), which also contributes to the reduction in emittance. Consequently, at the exit of the RFQ the HOMB has an emittance much less than that of the Gaussian beam. However, the difference in the longitudinal emittance for the Gaussian and HOMB along the RFQ is not as noticeable as the transverse.

To better understand the nonlinear beam dynamics that leads to halo formation and beam loss, we tracked the trajectories of individual particles, identified the lost particles, and plotted their initial coordinates, Fig. 10. Even without mismatch, Fig. 10(a), the Gaussian distribution shows beam loss from the centre as well as the outer lobes, whereas the HOMB, Fig. 10(b), shows particle loss only from the center. With a mismatch of 30% the beam loss is obviously much more. For the Gaussian beam,

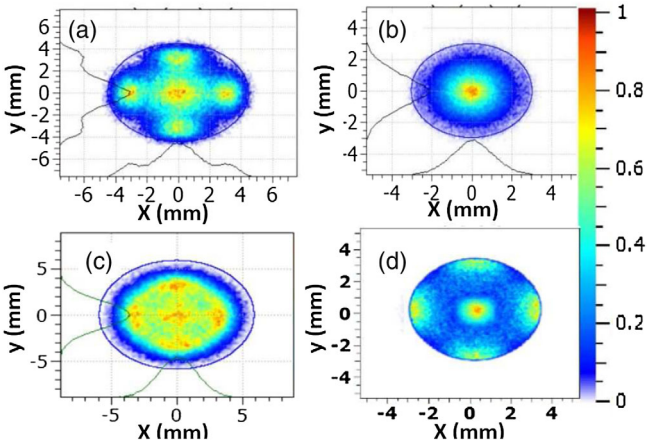

FIG. 10. Initial distribution of the lost particles for the (a) Gaussian, and (b) HOMB, with zero initial mismatch, and for the (c) Gaussian and (d) HOMB, with 30% mismatch.

Fig. 10(c), particle loss away from the center is much more, and even the HOMB, Fig. 10(d), picks up some loss from radial lobes. In either case, however, for the HOMB the density of lost particles is maximum at the center, whereas for the Gaussian beam the density is maximum at the center as well as at the outer lobes. Since for the HOMB the particle density near the beam center is already low, the percentage of lost particles automatically goes down. This explains why the HOMB has less beam loss compared to the Gaussian. With 30% mismatch, for example, beam loss is 11% for the HOMB and 20% for the Gaussian.

In order to compare with the predictions of the particle-core model we calculated the tunes (oscillation frequencies) of individual particles (through FFTs), as well as the envelope oscillation frequency, without mismatch and for a mismatch of 30%. Figures 11(a) and 11(b) show that, without mismatch, the tunes of many transversely lost particles are indeed clustered at a frequency that is half the envelope frequency (dashed lines), in agreement with the particle-core model. For the HOMB [Fig. 11(b)] all the transversely lost particles are clustered at this tune while for the Gaussian beam [Fig. 11(a)] some lost particles have very different tunes—they are clustered around nonlinear transverse resonances. Longitudinally lost particles also have very different tunes, for both the Gaussian and HOMB, since their loss cannot be described by the particle-core model. With mismatch, the situation is exacerbated. For the HOMB [Fig. 11(d)] most transversely lost particles are still clustered along the parametric resonance, but for the Gaussian beam [Fig. 11(c)] the number of transversely lost particles that are clustered around nonlinear resonances has significantly increased. The number of longitudinally lost particles has not changed substantially due to mismatch, which is not surprising since the mismatch is only in the transverse dimensions.

One can try to identify the nonlinear resonances that are causing beam loss for the Gaussian beam [Fig. 11(c)]. The

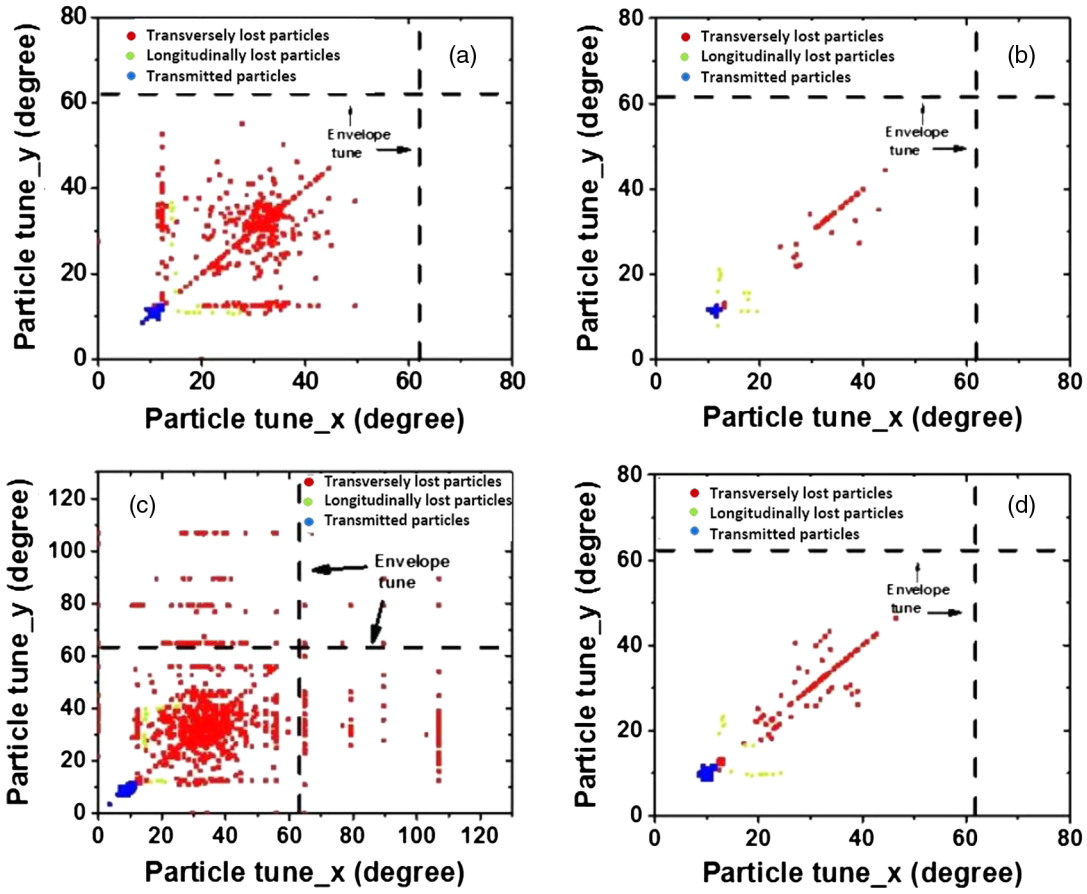

FIG. 11. Plots of the x-y tunes of lost particles, (a) Gaussian beam, no mismatch, (b) HOMB, no mismatch, (c) Gaussian beam, 30% initial mismatch, (d) HOMB, 30% initial mismatch.

resonance at 90° can be identified as the fourth-order resonance $4\sigma = 360$, where σ is the depressed phase advance of the particle, or equivalently as $4Q = 1$ [38–40], where Q is the fractional tune of the particle. Similarly, the resonance at 60° can be identified as $6Q = 1$ [41]. Then there are even higher-order resonances. The one at 106° can be identified as the $7Q = 2$ resonance, the one at 64° as the $11Q = 2$ resonance, and so on.

Thus, for the HOMB, in which the space-charge force is close to linear, the particle-core model, which assumes a linear space-charge force, agrees very well. For the Gaussian beam, however, the nonlinearity of the space-charge force is significant, and leads to loss mechanisms not described by the particle-core model. These losses are driven by nonlinear resonances that are excited more strongly as the degree of mismatch increases. Note also that the tunes of the transmitted particles are all clustered together at a much lower frequency, away from the parametric resonance and nonlinear resonances, and they are not very different for the Gaussian or HOMB, with or without mismatch.

We have also checked that the lost particles that originate from the off-center lobes in Fig. 10, all have tunes that fall along the nonlinear resonances, and therefore their loss is not explained by the particle-core model, whereas the lost particles that originate from the center have tunes that are roughly half the envelope tune, and their loss is well explained by the particle-core model. Further, Fig. 12 shows that particles that are driven by the nonlinear resonances are lost early in the RFQ, within the first 50 cm, whereas particles that are driven by the 1:2

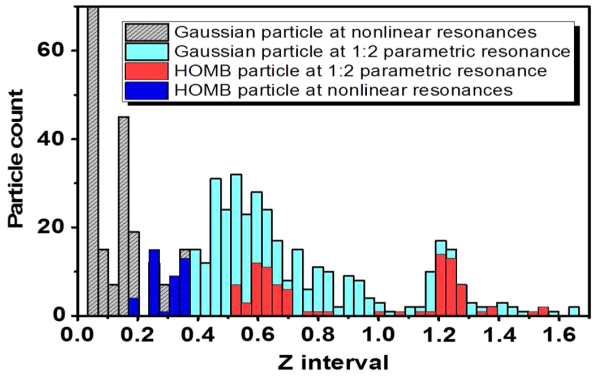

FIG. 12. Histogram of particle loss as a function of distance down the RFQ, for the Gaussian and HOMB, for a mismatch of 30%.

parametric resonance are lost much later, between around 0.5–1.5 m into the RFQ. This is true for the HOMB as well as the Gaussian, and is indicative of the fact that the parametric (1:2) and nonlinear resonances are two different mechanisms of particle loss.

IV. SEPARATRIX ANALYSIS

To better understand the motion of the particles, from the Hamiltonian point of view it is better to look at particle motion in phase space. To this end, we constructed the Hamiltonian from the two-term potential function [42] for the RFQ and the space-charge potential of the beam derived from the space-charge electric fields,

$$H = \frac{p^2}{2m} + V_{\mathrm{RFQ}} + V_{\mathrm{SC}}, \tag{10}$$

where,

$$V_{\mathrm{RFQ}}(r,z,t) = \frac{V_0}{2}\left[\frac{X}{a^2}(x^2 - y^2)\right] + \frac{V_0}{2}[AI_0(kr)\cos(kz)]\sin(\omega t). \tag{11}$$

Here X and A are functions of the modulation and aperture in terms of modified Bessel functions, V_{SC} is the space-charge potential for the input distribution, and $I_0(kr)$ is the lowest order modified Bessel function.

Tracking these particles in phase-space shows that they are getting some kick at a given longitudinal position and as a result their phase-space trajectory blows up and finally the particles hit the RFQ vanes (Fig. 13) but, as the potential seen by the particle is saddle shaped (Fig. 14), if the particle is lost in x, its trajectory would not blow up in y as it sees a potential hill in one dimension and a potential well in the other.

Figures 15 show how the x-coordinate of the particle varies as it is being accelerated. For a typical transmitted particle, Fig. 15(a), one can see that the particle's x-coordinate oscillates within fixed bounds. For a lost particle, however, Fig. 15(b) shows that as the particle is accelerated, the particle's x-coordinate varies irregularly, indicating stochastic behavior, until the particle is finally lost, at an energy of around 80 keV.

From Figs. 15(a) and 15(b) it seems that the transmitted particle is oscillating in a global potential with zero as its mean, whereas the lost particle does perform an oscillation about zero but at times it also jumps from one to another local mean position. This can be because it is trapped in some local potential and finally it is lost as the potential seen by the particle becomes unbounded. After looking at data for all the transmitted as well as lost particles individually, we observe the same chaotic trend in the trajectories of the lost particles and the transmitted are all well behaved as shown in Fig. 15.

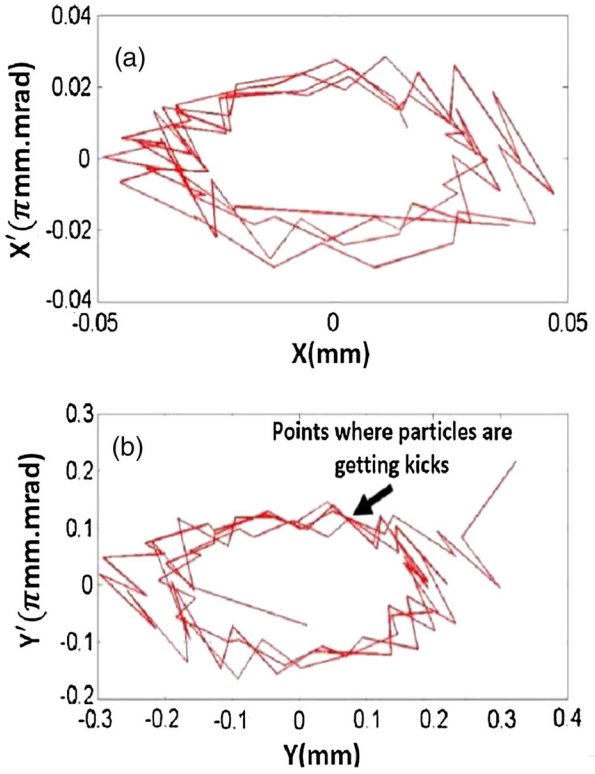

FIG. 13. Phase space trajectory of a lost particle along propagation direction in: (a) $xx\prime$ and (b) $yy\prime$. It can be seen that the particle remains confined in x but is lost in y.

From Hamiltonian dynamics one can describe the loss of particles as arising as a result of the energy of the particle increasing so that the particle falls out of the separatrix in phase space. As a consequence the particle is no longer trapped in an oscillatory potential, and is lost. To understand particle loss from this angle, we used the two-term potential of the RFQ along with the space-charge potential to calculate the separatrix at every half cell length ($\beta\lambda/2$) of the RFQ. To avoid the complexity in the system and still understand the process, we studied the particle dynamics along x and y (transverse) dimensions independently. For the

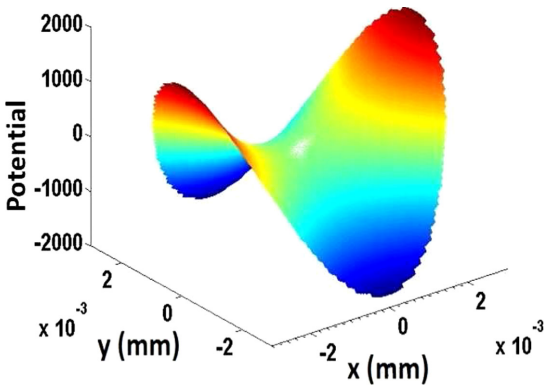

FIG. 14. RFQ potential at a given longitudinal position and at a given time. The potential is saddle-shaped, explaining the behavior seen in Fig. 13.

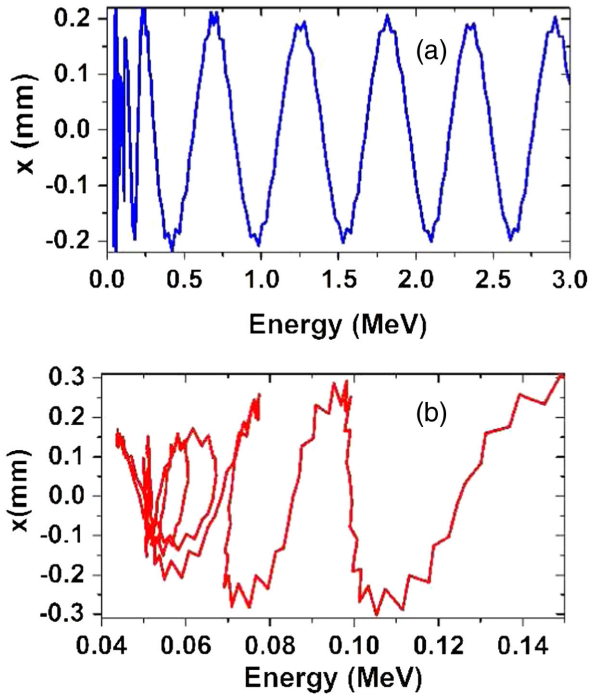

FIG. 15. x vs energy plot for the (a) transmitted, and (b) lost, particles.

Gaussian beam we calculated the space-charge potential from the analytic expressions for the fields by integration. For the HOMB we calculated the potential numerically using the successive overrelaxation (SOR) method. Assuming a value of the Hamiltonian, one can get the phase-space trajectory of the particle. By varying the value of the Hamiltonian, one can then trace out different trajectories, and, in particular, identify the trajectory corresponding to the separatrix. From this value of the Hamiltonian, one can calculate the transverse kinetic energy.

Figures 16 show a plot, in green, of this transverse (horizontal) energy of the separatrix, as a function of distance down the RFQ; Fig. 16(a) for the Gaussian beam and Fig. 16(b) for the HOMB. Also shown are the corresponding transverse energies for individual particles close to the x-axis (so that only the horizontal dynamics is important), as they travel down the RFQ. For the transmitted particles, shown in blue, their transverse energy is plotted at each longitudinal position, up to the end of the RFQ. It can be seen that at no time in their traversal through the RFQ does the energy of these particles cross the separatrix. For the lost particles, the energy at the longitudinal position at which the particle is lost is shown in red. Clearly, when a particle is lost, its energy is always greater than the separatrix. This validates the Hamiltonian analysis and explanation for the loss of particles in the RFQ. A comparison of Figs. 16(a) and 16(b) also shows clearly that there is more beam loss for the Gaussian beam compared to the hollow one. Further, the larger separatrix width for the hollow beam as compared to the Gaussian is also evident.

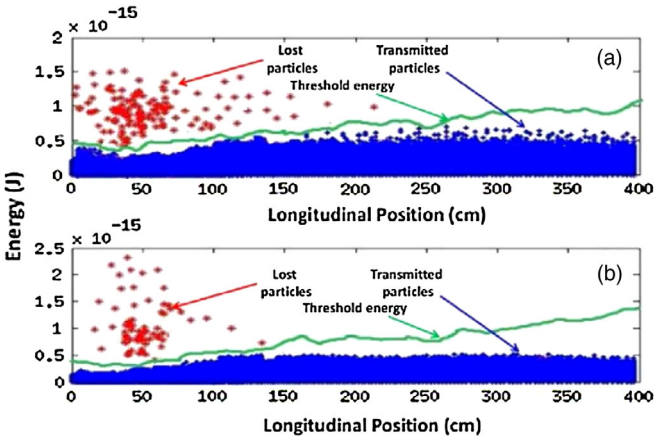

FIG. 16. Transverse threshold energy plot as a function of longitudinal position overlapped with particles transverse energy: (a) for the Gaussian beam and (b) for the HOMB.

V. CONCLUSION

In summary, our results show that a higher order Laguerre-Gauss beam (HOMB) can be naturally produced in the LEBT of a HIPL, and its transport through the RFQ produces much less emittance blow-up as well as halo formation and beam loss, as compared to a Gaussian beam. For the HOMB, where the space-charge force is more linear, the particle-core model fits quite well. Loss is mainly due to the 1:2 parametric resonance, and lost particles are mainly from the center of the beam. However, since the HOMB has fewer particles at the center, the emittance increase, halo formation and particle loss, are all much less for a HOMB than for a Gaussian. For a Gaussian beam there is an additional loss mechanism, in the form of nonlinear space-charge resonances, that is not predicted by the particle-core model. This mechanism is more important for the Gaussian beam, and results in larger rms emittance, larger beam halos, greater tune depression and greater beam loss.

Therefore, it would be advantageous to produce and transport a HOMB in high intensity proton linacs to achieve lower emittance, mitigated beam halos, and lesser beam loss. The reduction of beam halos at lower energy can also be expected to contribute to reduced beam loss at high energy, and therefore allow for higher beam intensity, which is essential for the successful implementation of ADRS.

[1] S. Henderson, Status of the SNS – Machine and Science, in *Proceedings of the 22nd Particle Accelerator Conference, PAC-2007, Albuquerque, NM* (IEEE, New York, 2007), p. 7.

[2] M. Eshraqi, M. Brandin, I. Bustinduy, C. Carlile, H. Hahn, M. Lindroos, C. Oyon, S. Peggs, A. Ponton, K. Rathsman, R. Calaga, T. Satogata, and A. Jansson, Conceptual design of the ESS linac, in *Proceedings of the International*

Particle Accelerator Conference, Kyoto, Japan (ICR, Kyoto, 2010), p. 300.

[3] High-intensity Proton Accelerator Project Team, JAERI Report No. JAERI-Tech 2003-044, 2003.

[4] J.-L. Biarrotte, S. Bousson, T. Junquera, A. C. Mueller, and A. Olivier, A reference accelerator scheme for ADS applications, Nucl. Instrum. Methods Phys. Res., Sect. A **562**, 656 (2006).

[5] M. Mizumoto, J. Kusano, K. Hasegawa, N. Ouchi, H. Oguri, M. Kinsho, E. Chishiro, T. Tomisawa, Y. Touchi, M. Ikegami, and Y. Honda, A high intensity proton linac development for the JAERI neutron science project, in *Proceedings of the 19th International Linear Accelerators Conference, Chicago, IL, 1998* (NTIS, Springfield, VA, 1998), p. 349.

[6] S. S. Kapoor, Accelerator-driven sub-critical reactor system (ADS) for nuclear energy generation, Pramana **59**, 941 (2002).

[7] R. L. Gluckstern, Analytic Model for Halo Formation in High Current Ion Linacs, Phys. Rev. Lett. **73**, 1247 (1994).

[8] G. Franchetti, I. Hofmann, and D. Jeon, Anisotropic Free-Energy Limit of Halos in High-Intensity Accelerators, Phys. Rev. Lett. **88**, 254802 (2002).

[9] C. K. Allen and T. P. Wangler, Parameters for quantifying beam halo, in *Proceedings of the Particle Accelerator Conference, Chicago, IL, 2001* (IEEE, New York, 2001), p. 1732.

[10] J. Gao, Internal Reports No. LAL-RT-2002-15, No. SIS-2003-181, 2002.

[11] M. Lund, M. Steven, J. J. Barnard, B. Bukh, S. R. Chawla, and S. H. Chilton, A core-particle model for periodically focused ion beams with intense space-charge, Nucl. Instrum. Methods Phys. Res., Sect. A **577**, 173 (2007).

[12] H. Qin, M. Chung, and R. C. Davidson, Generalized Kapchinskij-Vladimirskij Distribution and Envelope Equation for High-Intensity, Phys. Rev. Lett. **103**, 224802 (2009).

[13] J. Qiang, P. L. Colestock, D. Gilpatrick, H. V. Smith, T. P. Wangler, and M. E. Schulze, Macroparticle simulation studies of a proton beam halo experiment, Phys. Rev. ST Accel. Beams **5**, 124201 (2002).

[14] J. S. O'Connell, T. P. Wangler, R. S. Mills, and K. R. Crandall, Beam halo formation from space-charge dominated beams in uniform focusing channels, in *Proceedings of the IEEE Particle Accelerator Conference* (IEEE, Piscataway, 1993), p. 3657.

[15] T. P. Wangler, C. K. Allen, K. C. D. Chan, P. L. Colestock, K. R. Crandall, R. W. Garnett, D. Gilpatrick, W. Lysenko, J. Qiang, J. D. Schnieder, and M. E. Schulze, Experimental study of proton-beam halo induced by beam mismatch in leda, in *Proceedings of the Particle Accelerator Conference, Chicago, IL, 2001* (IEEE, New York, 2001), p. 2923.

[16] D. Jeon, J. Stovall, A. Aleksandrov, J. Wei, J. Staples, R. Keller, L. Young, H. Takeda, and S. Nath, Formation and mitigation of halo particles in the Spallation Neutron Source linac, Phys. Rev. ST Accel. Beams **5**, 094201 (2002).

[17] D.-O. Jeon, Evidence of a halo formation mechanism in the Spallation Neutron Source linac, Phys. Rev. ST Accel. Beams **16**, 040103 (2013).

[18] L. Groening, W. Barth, W. Bayer, G. Clemente, L. Dahl, P. Forck, P. Gerhard, I. Hofmann, G. Riehl, S. Yaramyshev, D. Jeon, and D. Uriot, Benchmarking of measurement and simulation of transverse rms-emittance growth, Phys. Rev. ST Accel. Beams **11**, 094201 (2008).

[19] J. Qiang and R. D. Ryne, Beam halo studies using a three-dimensional particle-core model, Phys. Rev. ST Accel. Beams **3**, 064201 (2000).

[20] T. P. Wangler, K. R. Crandall, R. Ryne, and T. S. Wang, Particle-core model for transverse dynamics of beam halo, Phys. Rev. ST Accel. Beams **1**, 084201 (1998).

[21] J. Qiang, R. D. Ryne, S. Habib, and V. Decyk, An object-oriented parallel particle-in-cell code for beam dynamics simulation in linear accelerators, J. Comput. Phys. **163**, 434 (2000).

[22] J. Qiang, R. D. Ryne, S. Habib, and V. Decyk, An object-oriented parallel particle-in-cell code for beam dynamics simulation in linear accelerators, in *Proceedings of the 1999 ACM/IEEE Conference on Supercomputing* (ACM, New York, 1999), p. 55.

[23] Y. K. Batygin, Particle-in-cell code BEAMPATH for beam dynamics simulations in linear accelerators and beamlines, Nucl. Instrum. Methods Phys. Res., Sect. A **539**, 455 (2005).

[24] J. Qiang, R. D. Ryne, B. Blind, J. H. Billen, T. Bhatia, R. W. Garnett, G. Neuschaefer, and H. Takeda, High-resolution parallel particle-in-cell simulations of beam dynamics in the spallation neutron source linac, Nucl. Instrum. Methods Phys. Res., Sect. A **457**, 1 (2001).

[25] N. Chauvin, O. Delferrire, R. Duperrier, R. Gobin, P. A. P. Nghiem, and D. Uriot, Transport of intense ion beams and space charge compensation issues in low energy beam lines, Rev. Sci. Instrum. **83**, 02B320 (2012).

[26] A. E. Siegmann, *Lasers* (University Science Books, Sausalito, 1986).

[27] P. Krejcik, Space charge limits in the acceleration of intense hollow beams, in *Proceedings of the 12th International Linac Conference, LINAC-1984, Seeheim, Germany, 1984* (GSI, Darmstadt, Germany, 1984), p. 352.

[28] P. Krejcik and R. Keller, A high-current beam transport facility for hollow beams, Vacuum **34**, 11 (1984).

[29] R. Pande, P. Singh, S. V. L. S. Rao, S. Roy, and S. Krishnagopal, Optimization of solenoid based low energy beam transport line for high current H+ beams, J. Inst. **10**, P02001 (2015).

[30] M. Reiser, *Theory and Design of Charged Particle Beams* (John Wiley & Sons, New York, 2008).

[31] D. A. Edwards and M. J. Syphers, *An Introduction to the Physics of High Energy Accelerators* (John Wiley & Sons, New York, 2008).

[32] D. Uriot and N. Pichoff, TraceWin, documentation, CEA/DSM/DAPNIA/SEA/2000/4 (2000).

[33] L. T. Sun, D. Leitner, G. Machicoane, E. Pozdeyev, V. Smirnov, S. B. Vorozhtsov, D. Winklehner, and Q. Zhao, Low energy beam transport for facility for rare isotope beams driver linear particle accelerator, Rev. Sci. Instrum. **83**, 02B705 (2012).

[34] Q. Zhao, X. Wu, V. Andreev, A. Balabin, M. Doleans, D1. Gorelov, T. L. Grimm, W. Hartung, D. Leitner, C. M. Lyneis, F. Marti, S. O. Schriber, and R. C. York, Beam simulation studies of the LEBT for RIA driver linac, in *Proceedings of 16th International Workshop on ECR Ion*

Sources, Berkeley CA, 2004, *AIP Conf. Proc.* 749, 242 (AIP, New York, 2005).

[35] V. Toivanen, G. Bellodi, D. Kchler, A. Lombardi, R. Scrivens, and J. Stafford-Haworth, Simulation of the CERN GTS-LHC ECR ion source extraction system with lead and argon ion beams, in *Proceedings of 21th International Workshop on ECR Ion Sources, Nizhny Novgorod, Russia, 2014* (Institute of Applied Physics, Nizhny Novgord, 2014), p. 23.

[36] I. M. Kapchinskii and V. V. Vladimirskii, Limitations of proton beam current in a strong focusing linear accelerator associated with the beam space charge, in *Proceedings of the International Conference on High Energy Accelerators and Instrumentation, 1959* (CERN, Geneva, 1959), p. 274.

[37] S. V. L. S. Rao and P. Singh, Design studies of a high-current radiofrequency quadrupole for accelerator-driven systems programme, Pramana **74**, 247 (2010).

[38] D.-O. Jeon, Experimental evidence of space charge driven resonances in high intensity linear accelerators, Phys. Rev. Accel. Beams **19**, 010101 (2016).

[39] L. Groening, W. Barth, W. Bayer, G. Clemente, L. Dahl, P. Forck, P. Gerhard, I. Hofmann, M. S. Kaiser, M. Maier, S. Mickat, T. Milosic, D. Jeon, and D. Uriot, Experimental Evidence of the 90° Stop Band in the GSI UNILAC, Phys. Rev. Lett. **102**, 234801 (2009).

[40] D. Jeon, L. Groening, and G. Franchett, Fourth order resonance of a high intensity linear accelerator, Phys. Rev. ST Accel. Beams **12**, 054204 (2009).

[41] D.-O. Jeon, K. R. Hwang, J.-H. Jang, H. Jin, and H. Jang, Sixth-Order Resonance of High-Intensity Linear Accelerators, Phys. Rev. Lett. **114**, 184802 (2015).

[42] T. P. Wangler, *RF Linear Accelerators* (John Wiley & Sons, New York, 2008).